Computational Aeroelastic Analysis of the Ares Launch Vehicle During Ascent

Robert E. Bartels
Pawel Chwalowski, Steven J. Massey, Jennifer Heeg*
Carol D. Wieseman†
NASA Langley Research Center, Hampton, VA, 23681, USA
Raymond E. Mineck‡
ViGYAN Inc., Hampton, VA, 23681, USA

This paper presents the static and dynamic computational aeroelastic (CAE) analyses of the Ares crew launch vehicle (CLV) during atmospheric ascent. The influence of launch vehicle flexibility on the static aerodynamic loading and integrated aerodynamic force and moment coefficients is discussed. The ultimate purpose of this analysis is to assess the aeroelastic stability of the launch vehicle along the ascent trajectory. A comparison of analysis results for several versions of the Ares CLV will be made. Flexible static and dynamic analyses based on rigid computational fluid dynamic (CFD) data are compared with a fully coupled aeroelastic time marching CFD analysis of the launch vehicle.

Nomenclature

B_{cfd}	Projection matrix, structure to CFD surface nodes
B_{ll}	Projection matrix, structure to section loads analysis points
$\hat{c}$	x,y,z non-dimensional force coefficients per unit vehicle length
c_{cr}	Critical structural damping ($2M_s\omega$)
c_s	Structural damping
c_a	Aerodynamic damping
Dia	Reference diameter
E	Young's modulus
f	Vector of forces at CFD node points
$\mathbf{F}$	Flow variable flux vector
$\mathbf{F}^*$	Flux vector for moving volume
g	Generalized variable
g_d	Dynamic component of generalized variable
g_s	Static component of generalized variable
G	Generalized force vector
G_s	Static component of generalized force vector
I	Identity matrix
M_s	Generalized structural mass
N_{cfd}	Number of CFD surface nodes
N_{ll}	Number of section nodes
N_s	Number of centerline structure nodes
$\mathbf{q}$	Vector of conserved flow variables
q_∞	Free stream dynamic pressure
q_{nom}	Free stream dynamic pressure at nominal ascent
S	Reference area
T	Thrust force magnitude
T_y	y transformation matrix

*Aerospace Engineer, Aeroelasticity Branch, Senior Member
†Aerospace Engineer, Aeroelasticity Branch, Associate Fellow
‡Senior Member

T_z z transformation matrix
U_∞ Free stream velocity
$\mathbf{W}$ Velocity of control volume surfaces
x_g x location of the engine gimbal
Δx x distance between section load points
α Vehicle angle of attack
α_l Local angle of attack
β Vehicle angle of sideslip
β_l Local angle of sideslip
γ_y Gimbal pitch angle
$\delta(x_g)$ Dirac delta centered at gimbal point
$\vec{\delta}_0$ Rigid body displacement vector
$\vec{\delta}_s$ Static aeroelastic displacement vector
$\vec{\delta}_d$ Dynamic aeroelastic displacement vector
Δ Structural and aerodynamic damping matrix
$\vec{\Delta}$ Total displacement vector
ε Strain tensor
ϕ Matrix of eigenvectors of structural dynamics equations
Φ_{cfd} Modal vectors projected to the CFD surface mesh
Φ_{ll} Modal vectors projected to the section loads analysis points
χ State variable vector
ζ_a Aerodynamic damping ratio (c_a/c_{cr})
ζ_s Structural damping ratio (c_s/c_{cr})
ζ_{ss} Static structural damping ratio
ζ_{sd} Dynamic structural damping ratio
λ, μ CFD grid pseudo material properties
ν Poisson ratio
ρ_∞ Freestream density
σ Stress tensor
τ Pseudo time
ω Modal frequency of vehicle structure
Ω Structural and aerodynamic stiffness matrix

Note to Readers: The predicted performance and certain other features and characteristics of the Ares I launch vehicle are defined by the U.S. Government to be Sensitive But Unclassified (SBU). Therefore, details have been removed from some plots and figures.

I. Introduction

The Vision for Space Exploration and the NASA Authorization Act of 2005 directed NASA to develop the technology to send astronauts back to the Moon and beyond to Mars. The Constellation program is tasked with developing the tools necessary to execute these next steps in the U.S space program. Within that program the Ares and the Orion projects develop the crew launch vehicle (CLV) and crew exploration vehicle (CEV) technology. The Ares project has the task of developing the vehicle necessary to launch the CEV and associated hardware to destinations beyond low earth orbit.

The engineering of the Ares CLV is a departure from past launch vehicles in that computational fluid dynamics (CFD) will be an integral part of the design from the conceptual stage. The vehicle will be designed with the smallest ever proportion of aerodynamic data derived from wind tunnel testing and the largest ever due to CFD. This approach to launch vehicle design poses both exciting possibilities in the extent to which the aerodynamics and flow field physics of a launch vehicle can be understood as well as challenges in validating methodologies for the highly complex flow field about a launch vehicle.

Aeroelastic stability has been a concern since early development of the Saturn I.[1,2] Vehicles with a hammerhead configuration, having a larger diameter upper stage, have the potential for aeroelastic instability.[3,4] One of the notable features of the Ares I and I-X is the use of a five segment Solid Rocket Booster (SRB) as a first stage with a

larger diameter upper stage. The two stages are connected by an aft-facing frustum. Along with the usual geometric complexity a major launch vehicle, this hammer-head configuration poses a challenge to CFD analysis because it has the potential of producing flow field separation from the frustum. Combined with shock separation over the upper stage, frustum separation can significantly influence overall vehicle aerodynamics.[3–5] In addition to the potential for shock and frustum separation, the first stage SRB aft skirt adds an additional mechanism for dynamic aeroelastic instability due to the disturbance time lag between the upper stage, frustum and the aft skirt.[4] These features of the Ares vehicle have motivated the wide spread use of high fidelity Navier-Stokes analyses, including a modeling of fluid/structure interaction, both static and dynamic, with a high fidelity Navier-Stokes flow solver.

A common method to simulate launch vehicle dynamics is the quasi-steady method of section loads. This approach models the displacement and inertial, elastic, and aerodynamic forces by a distribution along the vehicle centerline axis. The aerodynamic forcing is usually derived from steady state rigid aerodynamics, either from wind tunnel surface pressures or slender body theory. This model is based upon the assumption that, unlike lifting surfaces, the loading of a slender flexible launch vehicle can be approximated by a series of sectional loads each independently computed from rigid sectional aerodynamics. The model can be formulated in either the time or frequency domains. Combined with a model of vehicle buffeting or gust loading, this method provides a rapid simulation tool for the vehicle response dynamics during ascent. The origin of the method dates at least to Saturn I analyses,[2,6] and the aerodynamic modeling of section loads even earlier to slender body theory.[7] The vehicle structure typically is modeled as a simple beam.[3,4,8–10] This approach has been applied to launch vehicles[3,4,8], tactical weapons[9] and hypersonic atmospheric re-entry vehicles.[10] Recently, it has been applied to model the flight dynamics of a flexible slender launch vehicle in which a fourth order beam equation is developed that includes the effect of rigid body translational and rotational accelerations, with aerodynamics modeled from slender body theory.[11]

The limitation of the quasi-steady aeroelastic method of sectional loads is that it does not represent a true aeroelastic interaction of a vehicle in flight. The use of rigid steady aerodynamics assumes that each station along the body is influenced only by local angle of attack, and is not in any way influenced by flexibility induced down wash from upstream or downstream aerodynamic response to flexibility. Vehicle dynamics simulated by the quasi-steady aerodynamic method is further removed from reality, unless a correction is included to account for the phase shift due to the unsteady flow. The empirical method of Ericcson attempts to provide such a correction.

Ericsson has developed a quasi steady analytical method of sectional loads using steady state wind tunnel data that incorporates corrections to the aerodynamic damping based on an assumed disturbance time lag. This lag is due to the time required for boundary layer separation to grow in response to vehicle motion in an unsteady flow field compared to a steady flow field. The analytical/empirical approach of Ericsson does provide an initial rapid approximation to the phase shift,[3] and thus the destabilizing effect of unsteady aerodynamics. However, it is only approximate, and it is limited by the amount of data available. Never-the-less, Ericsson and Pavish suggest that an empirical method should be used first to assess the potential for instability.[4] If instability is indicated, additional unsteady CFD or wind tunnel studies are conducted.

To the authors' knowledge, the first attempts to provide unsteady CFD to launch vehicle analysis were performed by Azevedo[12]. This analysis tended to confirm the destabilizing effects predicted by the earlier analyses of Ericsson.[4] The use of CFD in the analysis of launch vehicles has expanded over the last several decades.[12–18] In the present work, we have initiated unsteady aeroelastic CFD early in the conceptual design stage. The goal is to provide an accurate analysis of aeroelastic vehicle stability early in the vehicle design.

NASA has employed a number of CFD codes, such as USM3D, to perform the aerodynamic analyses of the Ares I vehicles; however, only the unstructured CFD code FUN3D is being utilized for computational aeroelastic analysis. The aeroelastic analysis team has had at its disposal 9-10 million NAS core hours and 3-6 million core hours at a NASA Langley Research Center midrange computing cluster per year since Fiscal Year 08 to perform this analysis.

The present paper discusses two areas in which CAE analysis has been performed. The first is an understanding of the influence of flexibility on the vehicle's static loading and controllability. To quantify the static influence of flexibility, the flexible increments to the rigid longitudinal/lateral vehicle force and moment coefficients, as well as increments in aerodynamic loading due to thrust gimballing, are obtained. Current launch vehicle design typically uses rigid steady state wind tunnel force and moment coefficients and/or sectional load data based on rigid vehicle aerodynamics. The present paper adds to this design approach one that incorporates a full fluid/structure interaction. This paper will compare results derived by a fully coupled fluid/structure CAE analysis method and a quasi-steady method of section loads.

A second purpose of this effort is to assess the dynamic aeroelastic stability of the launch vehicle. Although a launch vehicle without fins does not have the potential for flutter of a lifting surface, it can experience dynamic aeroelastic instability and buffeting. Design practice requires that a launch vehicle be free of flutter beyond 1.32 times the nominal ascent dynamic pressure.[19] If an aeroelastic analysis shows dynamic aeroelastic instability within this range, aeroelastic wind tunnel testing is required and ultimately a flutter clearance of the vehicle. In response to this

requirement, a complete range of analyses have been conducted, an eigenvalue analysis using the quasi-steady method of section loads, a time marching dynamic aeroelastic analysis and a reduced order modeling (ROM) based on system identification of the launch vehicle aerodynamics. The ROM analyses for the Ares I vehicles will be discussed in a separate paper.[20] The current paper focuses on the quasi-steady section loads and time marching dynamic aeroelastic methods. The present analysis assumes that there are no rigid body rotational accelerations and also considers only the influence of transverse flexiblity.

The aeroelastic assessment of the Ares I-X flight test vehicle or Ares I crew launch vehicle requires analyses over the entire ascent trajectories. The trajectories of the two vehicles have subtle differences due to differing weights and aerodynamics. Figure 1 shows the Ares I lunar ascent trajectory with dynamic pressure in terms of vehicle Mach number. The symbols represent the analysis points. Static and dynamic aeroelastic results using FUN3D will be presented at these conditions. Selected conditions are also chosen to compare full aeroelastic interaction using FUN3D with quasi-steady section loads results.

II. Methods of Analysis

A. FUN3D Aeroelastic Solver

The Navier-Stokes code used in this study is FUN3D. The Fully Unstructured Navier-Stokes Three-Dimensional (FUN3D) flow solver is a finite-volume unstructured CFD code for either compressible or incompressible flows.[21,22] Flow variables are stored at the vertices of the mesh. FUN3D can solve the discrete compressible Euler or Reynolds-averaged Navier-Stokes (RANS) flow equations either tightly or loosely coupled with a turbulence model on mixed element grids, including tetrahedra, prisms and hexahedra. In the present study the RANS solver and the loosely coupled Spalart-Allmaras turbulence model are used on a tetrahedral grid.[23] FUN3D employs an implicit upwind algorithm in which the inviscid fluxes are obtained with a flux-splitting scheme. At interfaces delimiting neighboring control volumes, the inviscid fluxes are computed using an approximate Riemann solver based on the values on either side of the interface. Interface values are obtained by a least squares extrapolation using gradients computed at the vertices. Reconstruction requires limiting for flows with strong shocks.

A variety of gradient limiters are available. In the present study the low dissipation flux splitting scheme for the inviscid flux construction and the blended Van Leer flux limiter[24] were used. For tetrahedral meshes the full viscous fluxes are made discrete by using a finite-volume formulation in which the required velocity gradients on the dual faces are computed using the Green-Gauss theorem.[25] This approach is equivalent to a Galerkin type approximation. The solution at each time step is updated with a backwards Euler time differencing scheme and the use of local time stepping. At each time step, the linear system of equations is approximately solved either with a multi-color point-implicit procedure or an implicit-line relaxation scheme.[26] Domain decomposition exploits the distributed high-performance computing architectures that are necessary for the grid sizes used in the present study.

For a moving mesh, the conservation equations are written in the Arbitrary Lagrange Euler (ALE) formulation.[27] The unsteady Navier-Stokes equations written in integral form for a moving control volume are

$$\frac{\partial}{\partial t}\int_V \mathbf{q}\,dV + \int_{\partial V}(\mathbf{F}^* - \mathbf{F}_v)\cdot\hat{\mathbf{n}}\,dS = 0 \tag{1}$$

For a moving mesh the flux through the control volume is $\mathbf{F}^* = \mathbf{F} - \mathbf{q}\mathbf{W}^T$ where $\mathbf{F}$ is the flow variable flux vector associated with a stationary control volume. The vector $\mathbf{q}$ is the vector of conserved variables and the vector $\mathbf{W}$ represents the velocity of the local control volume surfaces. Additional information on the FUN3D implementation of the ALE formulation is found in reference[27].

The mesh deformation is accomplished by treating the mesh motion as analogous to a linear elasticity problem.[28] The linear elasticity equations written in differential form are

$$\nabla\cdot\sigma = 0 \tag{2}$$

where the stress tensor is given by $\sigma = \lambda Tr(\varepsilon)\mathbf{I} + 2\mu\varepsilon$ where Tr is the trace, $\mathbf{I}$ is the identity tensor, λ and μ are material properties and ε is the strain tensor. By use of the Gauss divergence theorem the elasticity equations can be written in finite-volume form and evaluated in a manner similar to the integration of the conservation form of the flow equations. The material properties vary based on distance to the nearest solid boundary. In contrast to the original implementation[28] in which the Poisson ratio is varied, elements near a solid boundary are made significantly stiffer by specifying the value of the Young's modulus (E). The Poisson ratio ν is given a uniform value of zero. The displacements are computed from the finite volume formulation of the elasticity equations using the Generalized Minimum Residual (GMRES) algorithm.[27,29]

In the present aeroelastic analysis FUN3D utilizes a modal decomposition of the structural model. An orthogonal transformation of the finite element equations provides the eigenvalues and eigenvectors from which the mode shapes and structural frequencies are derived. The transformed equations of elastic structural dynamics are

$$[I]\{\ddot{g}\} + [2\zeta_s \omega]\{\dot{g}\} + \left[\omega^2\right]\{g\} = q_\infty \left[\Phi_{cfd}\right]^T \{f\} \tag{3}$$

where

$$\left[\Phi_{cfd}\right] = \left[B_{cfd}\right][\phi] \tag{4}$$

and $\left[B_{cfd}\right]$ is a $3N_s \times 3N_{cfd}$ projection matrix relating structural centerline nodes to CFD surface nodes, $[\phi]$ is a $N_{modes} \times 3N_s$ matrix of eigenvectors and , $\left[\Phi_{cfd}\right]$ is a $N_{modes} \times 3N_{cfd}$ matrix of mode shapes projected to the CFD surface nodes.

B. Static and Dynamic Aeroelastic Analysis Based on Section Loads

The present paper formulates a flexiblized rigid integrated line loads (FRILLS) method that uses integrated surface pressures derived from rigid steady CFD coupled with a vehicle structural dynamics model that has been reduced to the vehicle centerline. Unlike previous quasi-steady sectional loading methods based on beam theory, the present method uses a Guyan reduction to the centerline of the full stack vehicle finite element model. This approach is fully compatible with the Guyan reduction also used in the FUN3D aeroelastic solutions. Compatibility of the two solution methods allows mixing models to perform rapid parametric studies of the influence of aeroelasticity on the system. By comparing FUN3D CAE with FRILLS solutions, we have a way to assess the effect of a full aeroelastic interaction on the static and dynamic responses of the vehicle.

The essence of the FRILLS method is to simplify the aeroelastic response of the vehicle to displacements along the vehicle centerline axis and apply elastic, inertial and aerodynamic forces at uniformly distributed points along that axis. Figure 2 shows the Ares I vehicle with the coordinate system superimposed. The vehicle is partitioned into N_{ll} stations. Displacements at each station can be written as a sum of rigid body displacements, static aeroelastic and dynamic aeroelastic displacements. In this analysis the rigid body displacements are considered to be zero. The displacement is defined $\vec{\Delta} = (\Delta_{1x}, \Delta_{1y}, \Delta_{1z}, \cdots, \Delta_{N_{ll}x}, \Delta_{N_{ll}y}, \Delta_{N_{ll}z})^T$ where

$$\vec{\Delta} = \vec{\delta}_s + \vec{\delta}_d \quad , \quad \vec{\delta}_s = f(x) \quad , \quad \vec{\delta}_d = f(x,t) \tag{5}$$

$\vec{\delta}_s$ and $\vec{\delta}_d$ are the static and dynamic aeroelastic centerline displacements, respectively, as functions of vehicle x-station and time, t. The material derivative yields an approximation for the local angles of attack and side slip

$$\{\alpha_l\} \approx \alpha + \frac{1}{U_\infty}[T_z]\{\frac{\partial \vec{\delta}_d}{\partial t} + U_\infty\left(\frac{\partial \vec{\delta}_s}{\partial x} + \frac{\partial \vec{\delta}_d}{\partial x}\right)\} \quad , \quad \{\beta_l\} \approx \beta + \frac{1}{U_\infty}[T_y]\{\frac{\partial \vec{\delta}_d}{\partial t} + U_\infty\left(\frac{\partial \vec{\delta}_s}{\partial x} + \frac{\partial \vec{\delta}_d}{\partial x}\right)\} \tag{6}$$

where matrices $[T_y]$ and $[T_z]$ are defined in the Appendix.

The mode shapes from the finite element model are projected to the analysis points along the vehicle. The projection can be written

$$[\Phi_{ll}] = [B_{ll}][\phi] \tag{7}$$

where $[B_{ll}]$ is an $3N_s \times 3N_{ll}$ projection matrix relating structural and sectional centerline nodes, and $[\Phi_{ll}]$ is a $N_{modes} \times 3N_{ll}$ matrix of mode shapes projected to the sectional centerline nodes. The matrices $[B_{ll}]$ and $\left[B_{cfd}\right]$ use the same method of projection to ensure consistency of the sectional load and FUN3D CAE results. The modal transformation yields

$$g = g_s + g_d = [\phi]^T [B_{ll}]^T \left(\vec{\delta}_s + \vec{\delta}_d\right) \tag{8}$$

where g_s is the generalized variable due to static loading and g_d is the generalized variable responding to vehicle dynamic forcing. The generalized forcing due to aerodynamics can be written in terms of the $3N_{ll}$ dimensional section loading $\hat{c}$

$$G = \frac{q_\infty S \Delta x}{Dia}[\phi]^T [B_{ll}]^T \hat{c} \tag{9}$$

where

$$\hat{c} = (\hat{c}_{1x} \quad \hat{c}_{1y} \quad \hat{c}_{1z} \quad \cdots \quad \hat{c}_{N_{ll}x} \quad \hat{c}_{N_{ll}y} \quad \hat{c}_{N_{ll}z})^T \tag{10}$$

The aerodynamic loading at each body station n, $\hat{c}_{nx}$, $\hat{c}_{ny}$, $\hat{c}_{nz}$ is a function of Mach number, angle of attack and angle of side slip. Representative data sets of z direction section loads as a function of angle of attack (at $\beta = 0$) are shown in

Figure 3. The FUN3D section loads data set has data at intervals ($\Delta\alpha$ and $\Delta\beta$) of 0.25 degrees from -1 to 5 degrees. The USM3D data is at intervals of 4 degrees from 0 to 8 degrees.

The sectional aerodynamics are computed by integrating nondimensional pressure coefficients from the vehicle surface using the FUN3D and USM3D codes. The integration is accomplished using a discrete data transfer algorithm developed by Samareh.[30] The approach is based on that of Farhat, Lesoinne and LeTallec,[31] which is a variation of the inverse isoparametric method (IIM). The further modified IIM algorithm of Samareh[30] maintains conservation of momentum and energy between separate meshes having dissimilar mesh spacing by an integration of loads on the source mesh and injection of the force vectors to the target mesh. Having transferred discrete loads from the unstructured CFD mesh to the sectional mesh, the nodal loads are integrated into sectional loads. The sectional loads are assembled by computing CFD solutions for the rigid vehicle at each Mach number at a series of angles of attack and sideslip. Aerodynamic section loading along the vehicle body from this series of solutions is input to the present analysis. To facilitate the following analysis, $N_{ll} \times N_{ll}$ square matrices $[\hat{c}]$, $\partial[\hat{c}]/\partial\alpha$ and $\partial[\hat{c}]/\partial\beta$ are constructed placing along the diagonals the values of $\hat{c}$ or its derivatives. The derivatives with respect to α and β are computed from a spline fit of the aerodynamic section loadings.

Computation of the static aeroelastic solution using sectional loads can be performed by treating the structural dynamics in pseudo time τ. The equations of elastic structural dynamics can be written

$$[I]\{g_s\}'' + [2\zeta_{ss}\omega]\{g_s\}' + \left[\omega^2\right]\{g_s\} = G_s \tag{11}$$

where $()'$ indicates differentiation with respect to τ. The generalized aerodynamic forcing G_s is updated at each iteration using the current α_l and β_l. The static structural modal damping ζ_{ss} and dilation of pseudo time τ are set to optimize convergence of the static solution.

The dynamic response of the vehicle can be computed by linearizing the line loads around the local static α_l, β_l and static generalized force G_s. The linearized equation can be written

$$[I]\{\ddot{g}_d\} + [\Delta]\{\dot{g}_d\} + [\Omega]\{g_d\} = 0 \tag{12}$$

where

$$[\Omega] = \left[\omega^2\right] - \rho_\infty {U_\infty}^2 [Q_k] \qquad , \qquad [\Delta] = [2\zeta_{sd}\omega] - \rho_\infty U_\infty \left[Q_\zeta\right] \tag{13}$$

$$\left[Q_\zeta\right] = \frac{S\Delta x}{2Dia}[\phi]^T [B_{ll}]^T \left\{ \frac{\partial[\hat{c}]}{\partial\alpha}\left[\hat{S}\right][T_z] + \frac{\partial[\hat{c}]}{\partial\beta}\left[\hat{S}\right][T_y] \right\} [B_{ll}][\phi] \tag{14}$$

and

$$[Q_k] = \frac{S\Delta x}{2Dia}[\phi]^T [B_{ll}]^T \left\{ \frac{\partial[\hat{c}]}{\partial\alpha}\left[\hat{S}\right][T_z] + \frac{\partial[\hat{c}]}{\partial\beta}\left[\hat{S}\right][T_y] \right\} [B_{ll}] \left[\frac{\partial\phi}{\partial x}\right] \tag{15}$$

The matrices $\left[\hat{S}\right]$, $[T_y]$ and $[T_y]$ are defined in the Appendix. Equation 12 can be written in state space

$$\dot{\chi} = [A]\chi \quad , \quad \chi = \{g_d, \dot{g}_d\}^T \tag{16}$$

where

$$[A] = \begin{bmatrix} 0 & I \\ -\Omega & -\Delta \end{bmatrix} \tag{17}$$

The eigen analysis of this system provides aeroelastic damping and frequency at a given flight condition.

III. Models

A. CFD Mesh

The unstructured tetrahedral grids used in this study were created using VGRID.[32] Since computational analysis was performed for both the Ares I-X and Ares I, grids have been developed for each of these vehicles. The Ares I vehicle has evolved during this preliminary design stage through a succession of outer mold line (OML) definitions. For the present study, the Ares I a105 OML was used. Four Ares I grids were developed, designated the extra coarse, coarse, baseline and fine.[33] The extra coarse grid had 10 million nodes, the coarse grid had 19 million nodes, the baseline had 41 million nodes and the fine grid had 83 million nodes. Several grids were also developed for the Ares I-X that are similar in size to the extra coarse, coarse and baseline Ares I grids. For each of these grids clustering at protuberances, rings and other geometric discontinuities was used to aid in resolving flow features. In the case of the Ares I, the refinement of successive grid levels was accomplished by doubling the number of surface nodes uniformly everywhere. A similar but somewhat less rigorous refinement strategy was used for the Ares I-X. The boundary layer

spacing normal to the vehicle surface was kept unchanged from one grid level to the next. Before performing the CAE analysis to be discussed presently, a study of the acceptable level of grid convergence was performed. Based in part on the results of this grid study and also the computational expense, the coarse level grid was used for many of the computations performed here. Refinement studies using the finer grids were done for a few critical cases in the transonic Mach number range. Additional details about the grid development and refinement studies for the Ares I are discussed in a separate paper.[33]

B. Structural Model

The structural models used in the Ares I-X and Ares I analyses are *MSC.Nastran*^{TM} finite element models. The Ares I-X model is designated Integrated Vehicle Model 12 (IVM12). Two Ares I models were used in the present analysis. The baseline Ares I model is designated Ares I Integrated Model 1 (AIIM1). The second Ares I model is otherwise identical but includes a upper stage Thrust Oscillation Isolator (AIIM1-TOI). The Ares I-X model includes a finite element modeling of the first stage, first stage solid propellant, second stage mass simulator, the Crew Exploration Vehicle (CEV) simulator and the Launch Abort System (LAS) simulator. The Ares I model includes a finite element modeling of the first stage, first stage solid propellant, second stage including liquid fuel and oxidizer masses, the CEV and LAS.

The Orion configuration utilized in the present Ares I analysis is the liftoff configuration for the lunar mission. The Orion structural data consists of a stiffness matrix produced by Craig-Bampton analysis, retaining information only along the centerline and an interface circumference where the Orion connects to the upper stage. The upper stage configuration contains fluid elements, pressure stiffening, and temperature effects associated with the Wetchill state of the J-2X engine. The first stage solid propellant is modeled as four concentrated masses. Because the first stage propellant mass changes during atmospheric ascent there is a continuous change in the stiffness and mass properties of the first stage. First stage propellant mass data was defined at a rather coarse spacing of ascent times, namely at 0, 20, 40, 50, 60, 80, 100 to 115 seconds. The lunar mission trajectory data, including total vehicle mass is defined significantly more finely. To apply propellant mass data in a consistent manner the coarsely spaced propellant data was interpolated to the present analysis points by matching total mass with the trajectory vehicle mass.

An additional Ares I structural model is used in the present analysis that incorporates a Thrust Oscillation Isolator (AIIM1-TOI). The AIIM1-TOI model is a dual plane isolation system intended to isolate the upper stage from first stage thrust oscillation. The isolator mechanism was modeled by a circumferential ring of springs at the interface between the Orion and the upper stage, and a circumferential ring of spring elements and mass elements at the interface between the upper stage and the first stage. In all other respects the AIIM1-TOI model is identical to the baseline Ares I structural model.

The entire Ares I vehicle structural model was reduced to 51 points along the vehicle centerline by a Guyan reduction. This reduction to the centerline produced both translational and rotational modal deflections. Since the focus of the present analysis is the influence of transverse deflections on vehicle stability, mode shapes having only axial or rotational deflections were discarded. Likewise, since other CFD analyses are intended to provide rigid vehicle data, rigid body modes were also not included in the present analysis. The remaining modes were ranked by the moduli of the mode shape amplitude and the top 44 flexible modes for the Ares I-X and 37 flexible modes for the Ares I were retained. The translational deflections of the remaining modes were projected with a spline fit to the CFD surface mesh points.

The liftoff frequencies of the retained modes span from 1.3 to 21.6 Hz for the Ares I-X and from 1.0 to 39 Hz for the Ares I. The difference in the upper bound in frequency is due to a better process of elimination of needless modes in the Ares I analysis. As SRB propellent is burned vehicle mass decreases and the frequencies of propellent related modes change. The first bending mode frequencies increase by 15-25 percent over the ascent. Mode switching also occurs. An analysis of the modal frequencies through the entire ascent showed that by including 37 to 44 modes, none of the important modes were lost to modal switching. The fact that the Ares I vehicle is more flexible than the Ares I-X is indicated in the relative frequencies of the first mode of each vehicle. Because of the additional springs located in the upper stage, the first mode frequencies of the Ares I AIIM1-TOI model are slightly lower still than that of the AIIM1 model. The orientation of the x, y, z coordinate system with respect to the vehicle is shown in Figure 2. The transverse y and z components of the coupled first two modes of the Ares I AIIM1 model are shown in Figure 4. These modes have an identical frequency but orthogonal modal amplitudes. Together they compose the first bending mode. For both vehicles, many modes over the entire frequency range exhibit similar pairing.

The finite element structural models per se do not include information about the structural damping. The preliminary design of the Ares I has relied in historical data to provide estimates. Hanson and Doggett measured the Saturn I wind tunnel model structural damping ratio ($\zeta_s = C_s/C_{cr}$) in the range 0.007 to 0.018.[7,34] Subsequent models and full scale estimates of Apollo/Saturn structural damping ratio were put at 0.012 to 0.022.[1] In the present aeroelastic

analysis an assumed nominal structural damping ratio value of 0.005 is used for all modes throughout the ascent. This value of damping ratio is consistent with the conservative value of structural damping of the first bending mode assumed in previous studies.[4]

IV. Results

A. Aeroelastic Analysis Process

Aeroelastic analysis using the FUN3D software is generally performed as a multi-step process. It is expedient first to perform a rigid steady state CFD solution from which to start the code aeroelastically. Converging a steady state rigid solution eliminates the destabilizing effect of coupling non-physical numerical transients with the dynamic elastic behavior of the vehicle. From this starting point a static aeroelastic computation provides a steady state flexible vehicle solution. Within FUN3D there are several ways to compute aeroelastically, either by coupling with an external structural solver or by an internal path that uses a modal representation of the structure. The present aeroelastic computations use the internal aeroelastic path. If a dynamic flexible analysis is desired, the starting point is the converged static aeroelastic solution. Starting a dynamic aeroelastic stability simulation from a static aeroelastic solution eliminates undesireable transients that otherwise clutter the dynamic response of the structure. The structural motion is excited by perturbing it with an initial generalized velocity. In this analysis, the time step for dynamic analyses has been selected to provide 700-1000 time steps per cycle for the first flexible mode and approximately 30 time steps per cycle for the highest frequency mode. The number of subiterations is set to fifteen.

B. Static Aeroelastic Results

Maintaining launch vehicle stability requires a guidance/navigation and control (GNC) system to correct for out-of-trim caused by aerodynamic and/or inertial forces. The design of the control system requires a prediction of the aerodynamic and inertial forcing. The rigid vehicle aerodynamics is supplied either by wind tunnel data and recently also CFD analysis. In addition to the aerodynamics of the rigid vehicle, typically static increments in the total vehicle force and moment are applied to account for flexibility. To provide this data, static aeroelastic analyses have been performed for both the Ares I-X and Ares I. Static aeroelastic solutions have been obtained at several angles of attack through fourteen ascent conditions for the Ares I-X and twenty conditions for the Ares I. Along with force and moment increments, the center of pressure shift is an important indicator of the relative impact of flexibility at various points in the ascent. The present analysis calculates the nondimentional aeroelastic center of pressure increment by

$$(\Delta c.p.)_{ae} = \frac{1}{Dia}\left((\frac{C_{my}}{C_z})_{flex} - (\frac{C_{my}}{C_z})_{rig} \right) \tag{18}$$

Positive shift is forward on the vehicle. The aeroelastic center of pressure increment for the Ares I at three grid levels has been computed at a subset of Mach numbers. Results of the grid study are shown in Figure 5. Coarse grid solutions are computed at all twenty conditions, baseline grid solutions are computed at Mach 0.50, 0.90, 1.00, 1.20 and 1.55, and fine grid solutions are computed at Mach 0.50 and 0.90. The major contributor to the shift in the center of pressure through the transonic range is the motion of the shock. The rapid positive trend in the Ares I aeroelastic center of pressure increment with Mach number is due to the formation of supersonic flow over the crew module. At low transonic Mach numbers this supersonic flow is terminated by a shock near the crew module. Aft movement of the shock from the crew module to the frustum with increasing Mach number between Mach 1.2 and 1.55 is the cause of the downward trend in the aeroelastic center of pressure increment over a very short Mach number range. Because of shock motion, the transonic Mach number range is substantially more sensitive to grid resolution than either the subsonic or supersonic ranges. At Mach 1.20 the solution on the baseline grid shows a significantly smaller shift than does the coarse grid solution. There is no fine grid solution at Mach 1.20, however at Mach 0.90 the center of pressure aeroelastic increment computed using the fine grid is still smaller. These results suggest that the coarse solution may over predict the change in the center of pressure in the transonic range.

Figure 6 shows the shift of the center of pressure due to flexibility of the Ares I-X compared with the Ares I. Both results are at $\alpha = 2.5$ degrees. The solutions are computed on comparible coarse grids. Each vehicle exhibits a forward movement of the center of pressure due to flexibility at this positive angle of attack throughout the entire ascent trajectory, and both show a peak in the forward shift of the center of pressure in the transonic to low supersonic range. Due to a stiffer upper stage and differences in the upper stage OML, the Ares I-X is influenced by flexibility to a lesser degree than the Ares I. The aeroelastic center of pressure increment in the transonic Mach range is significantly more pronounced for the Ares I. The aft motion of the Ares I-X shock, as deduced by the drop with increasing Mach number in the aeroelastic center of pressure increment, takes place at a lower Mach number than for the Ares I. After

the shock traverses the upper stage, the remaining ascent for each vehicle is accompanied with a much more benign change in aeroelastic center of pressure increment with inceasing Mach number.

A thrust force at a non-zero gimbal angle produces transverse deflection which in turn produces a change in the aerodynamic forces and moments. The resulting change in aerodynamic center of pressure is largely a function of the thrust force magnitude and gimbal angle and is influenced negligibly by dynamic pressure. An untrimmed thrust force will ordinarily produce a rotational acceleration. The present analysis imposed a point force to a free-free elastic model at the gimbal point with the rigid body degrees of freedom constrained. To this end the influence of the engine gimballing was included in both FUN3D aeroelastic and FRILLS simulations by adding an increment to the generalized force for each modal equation. An approximation of the contribution of the thrust force to the generalized force vector G is calculated in the present analysis by

$$G = \int T sin(\delta_g)(\Phi_{cfd})_z \delta(x_g) dx = T sin(\delta_g)(\Phi_{cfd})_z|_{x_g} \tag{19}$$

The orientation of the thrust force T and definition of gimbal pitch angle δ_g are shown in Figure 2. In the present analysis the x displacement of the vehicle due to thrust force is expected to have a negligible effect on lateral or longitudinal force and moment increments. The present calculation also uses the fact that modes having y and z components are largely decoupled from those having x components, and that the engine thrust is applied along the centerline of the vehicle. Figure 7 shows the shift in the center of pressure due to a 1 degree gimbal angle calculated with the coarse grid. The calculation producing these results was performed with a positive five degree thrust gimbal pitch angle for both the Ares I-X and Ares I. Both sets of results have been scaled to 1 degree to plot on a scale identical to the other plots shown here. The aeroelastic center of pressure increment due to thrust is shown for both the Ares I-X and the Ares I vehicles. The larger increment due to thrust for the Ares I is due to the greater flexibility of its upper stage in comparison with the Ares I-X. The Ares I thrust induced center of pressure increment is apparently sensitive to changes in vehicle pitch because the thrust increment at $\alpha = 5$ degrees is much lower than that at 2.5 degrees. The Ares I-X shows a much lower sensitivity to angle of attack.

Figure 8 shows presents the aeroelastic center of pressure increment calculated with the FRILLS method with and without trim. A comparison can be made of the aeroelastic center of pressure increment calculated with the FRILLS method with that due to the fully interactive aeroelastic method. FRILLS predicts the largest aeroelastic center of pressure increment at Mach 1.55 whereas the fully coupled aeroelastic solution puts it at Mach 1.2. The untrimmed FRILLS aeroelastic c.p. increment has a somewhat smaller peak in the aeroelastic center of pressure increment than does the fully coupled aeroelastic method. At Mach 4.5 the solutions by the two methods are very similar, whereas at Mach 0.5 the aeroelastic center of pressure increment due to the FRILLS method is somewhat higher. Figure 8 also shows the effect on the center of pressure of trimming the vehicle with engine thrust. The launch vehicle is trimmed by balancing the aerodynamic moment with the thrust, while aerodynamic forces remain untrimmed. The results with trim include the effect of vehicle transverse inertia relief and aerodynamics on the engine gimbal angle required for trim. At $\alpha = 2.5$ degrees, vehicle trim moves the center of pressure forward. The largest center of pressure movement is at Mach 1.20 with a value of approximately $0.2Dia$. This Mach number coincides with the largest center of pressure increment due to flexibility.

Static aeroelastic solutions have been computed at angles of attack of 0, 2.5 and 8 degrees. At an angle of attack in the vicinity of 0 degrees, it is impossible to calculate the aeroelastic center of pressure increment because the z force coefficient is close to zero. At an angle of attack of 2.5 the z force is sufficiently large to correctly compute the c.p. shift. The flexibility induced center of pressure increment at 2.5 and 8 degrees angle of attack is shown in Figure 9. At 8 degrees the aeroelastic center of pressure increment is much lower than at 2.5, but still positive. This result reflects the fact that shock strength and movement are less pronounced at the higher angle of attack than at a low angle of attack.

The remaining figures are intended primarily to compare the fully coupled aeroelastic CFD and the FRILLS methods. Both solutions are computed with the coarse grid. Figures 10 and 11 present the rigid force and pitch moment coefficients and their increments due to flexibility. The rigid force coefficients (Figure 10a) and rigid moment coefficients (Figure 11a) computed with the two methods match exactly. This comparison provides a check on the FRILLS computation as the two methods should give the same rigid results. The increment in force and moment coefficients due to flexibility (Figures 10b and 11b) computed with the two methods compare well at high supersonic Mach numbers. In the transonic range, even though the aeroelastic center of pressure increment computed with FRILLS (shown in Figure 8) compares moderately well with the full fluid/structure interaction, the force and pitch moment coefficients computed by the two methods do not compare well. In the aeroelastic FUN3D solution at Mach 1.20, flexibility of the vehicle causes increase in upward forcing on the vehicle in the crew module area and a downward shift in forcing in the aft skirt region. The net result of these changes is a decrease in upward force and an increase in pitch moment. On the other hand, the increments in force and moment computed with FRILLS are both strongly positive. This large

difference is a clear indication that in the transonic and subsonic Mach regions a fully coupled aeroelastic solution is required to capture the correct increments.

Figure 12 a) and b) are intended to compare static FRILLS results using USM3D rigid section loads data with the fully aeroelastic FUN3D results. The USM3D cell centered unstructured code is used to generate the rigid section loads and force and moment coefficient data used in the design of the Ares I. The USM3D results are computed on a significantly better refined grid than the FUN3D results. The USM3D data is computed for the Ares I a106 OML, whereas all other present FUN3D aeroelastic and FRILLS results are computed with the a105 OML. Despite slight differences in vehicle geometries and more significantly in grid resolution, both solutions show relatively similar trends in aeroelastic center of pressure increment at $\alpha = 2.5$ and 8 degrees in the transonic Mach range.

C. Dynamic Aeroelastic Results

Dynamic aeroelastic analyses have been performed to assess the aeroelastic stability of the Ares I-X and Ares I vehicles. To provide an initial assessment of overall aeroelastic characteristics of the vehicles, coarse grid dynamic computations were performed at all analysis conditions at $\alpha = 0$ and 2.5 at nominal trajectory conditions. At low subsonic Mach numbers the vehicles can have higher angles of attack. For that reason, at Mach 0.5, $\alpha = 5$ degrees was also included. The measurement of damping required excitation of a dynamic solution by an initial modal velocity. From the time histories the modal aerodynamic damping was computed. The log decrement method was applied to the first three or four cycles of oscillation.

The aeroelastic stability analysis of the Ares I-X revealed modal aerodynamic damping that was uniformly close to zero over the entire ascent. However, the Ares I proved to be somewhat more interesting dynamically. For that reason remainder of this paper will be devoted to the Ares I aeroelastic stability analysis. Figure 13 shows the minimum aerodynamic damping for the Ares I at each analysis point. The figure plots the ratio of aerodynamic modal damping to critical structural damping. At high supersonic and low subsonic Mach numbers the magnitude of damping of the least stable mode is small. In the transonic range there is a negative dip in damping, with the minimum at Mach 1.0.

Having identified the most critical Ares I condition to be at Mach 1.0 additional analyses are focused on understanding the behavior of the vehicle at that condition. A study of the effect of grid resolution on the aerodynamic damping was performed. Results are shown in Figure 14. In that and remaining figures left represents positive aerodynamic damping while right represents negative aerodynamic damping. Ares I modes 3 and higher show very little sensitivity to grid resolution. Mode 2 damping increases with grid resolution while mode 1 computed with the fine grid is much more undamped than with the other grids. The conclusion from this grid study is that even the fine grid does not show converged initial growth rates of the first mode oscillation.

Continuing the Mach 1.0 dynamic solutions further in time revealed the emergence of limit cycle oscillation in mode 1. Limit cycle oscillation appeared to be emerging in the solutions on all the grids although several were still showing slight growth or decay after eight to ten cycles. Figure 15 presents a time history of the first mode over twelve cycles computed with the fine grid. Amplitude dependent nonlinearity in the aerodynamics produces a change in the damping as the amplitude of the motion increases; undamping decreases to exactly counterbalance the structural damping. This finding is consistent with other launch vehicle data. Ericsson and Pavish show that aerodynamic damping due to shock dynamics can be at a minimum at $\alpha = 0$ degrees, and at lowest amplitudes of motion. As the amplitude increases, the experimental data show that the aerodynamic damping increases.[3] This trend is consistent with the present unsteady CFD results.

Figures 16 to 17 compare the damping of the fully coupled aeroelastic solutions with the FRILLS method. At all Mach numbers, the predicted damping of modes 3 and higher compare very well. At Mach 4.5 the damping of modes 1 and 2, computed by the two methods compare very well. At Mach 1.2 the comparison is somewhat less satisfactory. At Mach 1.0, shown in Figure 17, the two methods show damping values of modes 1 and 2 that are much different. The FRILLS method shows modes 1 and 2 strongly damped for both the AIIM1 and the AIIM1-TOI structural models. The dynamic FUN3D solutions shows mode 2 to be damped while mode 1 is undamped. It is also interesting to note that the AIIM1-TOI model shows a greater separation in damping of the two modes than does the AIIM1 model. The AIIM1-TOI model also shows a more negative modal aerodynamic damping in mode 1 than does the AIIM1 model.

Because the amplitudes of the Ares I modes 1 and 2 are nearly identical but orthogonal, it was of interest to investigate the cause of the difference in the damping of the two modes at Mach 1.0. The results of a study of the influence of OML on the dynamic aeroelastic behavior of the vehicle are shown in Figure 18(a and b). On the left is shown the damping of the original OML (with all protuberances) at q_{nom} (repeated from Figure 17b) and $1.32q_{nom}$. Figure 18b shows the damping from a computation using an clean OML with ring protuberances only; all other protuberances were removed. The damping of modes 1 and 2 of the clean OML are nearly identical. These results indicate that the reason for the strongly damped mode 2 and undamped mode 1 in the Ares I vehicle is the effect that protuberances have on the vehicle aerodynamics. Apparently an asymmetry in the locations of protuberances causes

the predominantly lateral mode 2 to be damped and the predominantly longitudinal mode 1 to be undamped.

V. Conclusions

This paper discussed two areas in which computational aeroelastic analysis has been performed in the support of developing the Ares I-X and Ares I launch vehicles. The first is an understanding of the influence of flexibility on static vehicle loading and controllability. In the transonic Mach range the Ares I vehicle displays considerable sensitivity of center of pressure aeroelastic increment to shock location and consequently the analysis is sensitive to grid resolution, angle of attack and free stream Mach number. Between Mach 1 and the maximum dynamic pressure condition there is a large positive center of pressure increment due to flexibility (positive forward). Through this Mach range, there is also a large and rapid change in the aeroelastic center of pressure increment with increasing Mach number. A second area was an assessment of the dynamic aeroelastic stability of the launch vehicle. The modal aerodynamic damping was computed from a log decrement of the time history of the fully coupled aeroelastic solutions. A complete range of analyses over the ascent trajectory have been presented, using a time marching dynamic aeroelastic analysis. In the transonic Mach range, the Ares I vehicle modal aerodynamic damping has a negative dip. The largest negative damping is at Mach 1. The AIIM1-TOI structural model, with its added isolator springs results in a more negative modal aerodynamic damping than the AIIM1 model. Selected conditions also were presented to compare a full aeroelastic interaction with results derived from a quasi-steady section loads. The modal aerodynamic damping values from a full aeroelastic interaction are compared with eigenvalues derived from the quasi-steady section loads method. Both static and dynamic aeroelastic results show that away from the transonic Mach range the two methods agree reasonably well. In the transonic range, the dynamic aeroelastic stability results calculated using the quasi-steady method do not agree well with those due to a fully coupled aeroelastic time marching CFD analysis. In either the static or dynamic sense, the method of quasi-steady section loads produces static and dynamic results that are somewhat to significantly unconservative. The present results suggests at the very least that through the transonic Mach range a method that provides the physically correct time accurate fluid/structure interaction is needed to predict dynamic flexible vehicle behavior.

Acknowledgments

The authors would like to acknowledge Pat Cosgrove and Paresh Parikh of the Ares Project Office for their support of this work. The authors wish to thank Khaled Abdol-Hamid of the Configuration Aerodynamics Branch, NASA Langley Research Center for providing the USM3D data used in this study.

References

[1]Hanson, P. W. and Doggett, R. V. J., "Aerodynamic Damping and Buffet Response of an Aeroelastic Model of the Saturn I Block II Launch Vehicle," NASA Technical Note NASA TN D-2713, 1965.

[2]Dogget, R. V. J. and W., H. P., "An Aeroelastic Model Approach for the Prediction of Buffet Bending Loads on Launch Vehicles," NASA Technical Note NASA TN D-2022, 1963.

[3]Ericsson, L. E. and Pavish, D., "Aeroelastic Vehicle Dynamics of a Proposed Delta II 7920-10L Launch Vehicle," *Journal of Spacecraft and Rockets*, Vol. 37, No. 1, 2000, pp. 28–38.

[4]Ericsson, L. E., "Aeroelastic Instability Caused by Slender Payloads," *Journal of Spacecraft*, Vol. 4, No. 1, 1967, pp. 65–73.

[5]Ericsson, L. E., "Unsteady Flow Separation Can Endanger the Structural Integrity of Aerospace Launch Vehicles," *Journal of Spacecraft and Rockets*, Vol. 38, No. 2, 2001, pp. 168–179.

[6]Ericsson, L. E. and Reding, J. P., "Report on Saturn I - Apollo Unsteady Aerodynamics," NASA Technical Note, LMSC-A650215 NAS 8-5338, 1964.

[7]Hanson, P. W. and Doggett, R. V. J., "Wind-Tunnel Measurements of Aerodynamic Damping Derivatives of a Launch Vehicle Vibrating in Free-Free Bending Modes at Mach Numbers from 0.70 to 2.87 and Comparisons with Theory," NASA Technical Note NASA TN D-1391, 1962.

[8]Blejwas, T. E., "Shuttle System Dynamic Loads Analysis," Contract Report, Martin Marietta NAS8-30635, 1975.

[9]Crimi, P., "Aeroelastic Stability and Response of Flexible Tactical Weapons," *22nd AIAA Aerospace Sciences Meeting*, No. 392, 1984.

[10]Oberholtzer, N. W., Schmidt, L. E., and Larmour, R. A., "Aeroelastic Behavior of Hypersonic Re-entry Vehicles," *21st AIAA Aerospace Sciences Meeting*, No. 33, 1983.

[11]Trikha, M., Mahapatra, D. R., Gopalakrishnan, S., and Pandiyan, R., "Analysis of Aeroelastic Stability of a Slender Launch Vehicle using Aerodynamic Data," *46th AIAA Aerospace Sciences Meeting*, No. 310, 2008.

[12]Scalabrin, L. C., Azevedo, J. L. F., Teixeira, P. R. F., and Awruch, A. M., "Three Dimensional Flow Simulations with the Finite Element Technique over a Multi-Stage Rocket," *40th AIAA Aerospace Sciences Meeting and Exhibit*, No. 408, 2002.

[13]Azevedo, J. L. F., "Aeroelastic Analysis of Launch Vehicles in Transonic Flight," *Journal of Spacecraft*, Vol. 26, No. 1, 1989, pp. 14–23.

[14]Bigarella, E. D. V., Basso, E., and Azevedo, J. L. F., "Multigrid Adaptive-Mesh Turbulent Simulations of Launch Vehicle Flows," *21st AIAA Applied Aerodynamics Conference*, No. 4076, 2003.

[15]Bigarella, E. D. V. and Azevedo, J. L. F., "Numerical Study of Turbulent Flows over Launch Vehicle Configurations," *Journal of Spacecraft and Rockets*, Vol. 42, No. 2, 2005, pp. 266–276.

[16]Scalabrin, L. C. and Azevedo, J. L. F., "Finite Volume Launch Vehicle Flow Simulations on Unstructured Adaptive Meshes," *41st AIAA Aerospace Sciences Meeting and Exhibit*, No. 601, 2003.

[17]Azevedo, J. L. F., "Aeroelastic Analysis of Launch Vehicles in Transonic Flight," *26th AIAA Aeroscience Meeting and Exhibit*, No. 708, 1987.

[18]Azevedo, J. L. F., "Aeroelastic Analysis of Hammerhead Payloads," *29th AIAA Structures, Structural Dynamics and Materials Conference*, No. 2307, 1988.

[19]"Flutter, Buzz, and Divergence, SP-8003," NASA Space Vehicle Design Criteria, 1964.

[20]Silva, W., Vatsa, V., and Biedron, R., "Reduced order models for the aeroelastic analysis of the Ares Vehicles," *28th AIAA Applied Aerodynamics Conference*, No. 4375, 2010.

[21]Anderson, W. K., Rausch, R. D., and Bonhaus, D. L., "An Implicit Upwind Algorithm for Computing Turbulent Flows on Unstructured Grids," *Computers and Fluids*, Vol. 23, No. 1, 1994, pp. 1–22.

[22]NASA LaRC, Hampton, VA, *FUN3D Manual*, Nov. 2008, http://fun3d.larc.nasa.gov.

[23]Spalart, P. R. and Allmaras, S. R., "One-Equation Turbulence Model for Aerodynamic Flows," *30th AIAA Aerospace Sciences Meeting and Exhibit*, No. 439, 1992.

[24]Vatsa, V. N. and White, J. A., "Calibration of a Unified Flux Limiter for Ares-Class Launch Vehicles from Subsonic to Supersonic Speeds," 56th Propulsion Meeting 5, JANNAF, III, April 2009.

[25]Rumsey, C. L. and Thomas, J. L., "Application of FUN3D and CFL3D to the Third Workshop on CFD Uncertainty Analysis," NASA Technical Memorandum NASA/TM-2008-215537, 2008.

[26]Nielsen, E. J., Lu, J., Park, M. A., and Darmofal, D. L., "An Exact Dual Adjoint Solution Method for Turbulent Flows on Unstructured Grids," *Computers and Fluids*, Vol. 33, No. 9, 2004, pp. 1131–1155.

[27]Biedron, R. T. and Thomas, J. L., "Recent Enhancements To The FUN3D Flow Solver For Moving-Mesh Applications," *47th AIAA Aerospace Sciences Meeting*, No. 1360, 2009.

[28]Nielsen, E. J. and Anderson, W. K., "Recent Improvements in Aerodynamic Design Optimiation on Unstructured Meshes," *AIAA Journal*, Vol. 40, No. 6, 2002, pp. 1155–1163.

[29]Saad, Y. and Schultz, M. H., "GMRES: A Generalized Minimum Residual Algorithm for Solving Nonsymmetric Linear Systems," *SIAM Journal of Scientific and Statistical Computing*, Vol. 7, 1986, pp. 856–869.

[30]Samareh, J. A., "Discrete Data Transfer Technique for Fluid-Structure Interaction," *18th AIAA Computational Fluid Dynamics Conference*, No. 4309, 2007.

[31]Farhat, C., Lesoinne, M., and LeTallec, P., "Load and Motion Transfer Algorithms for Fluid/Structure Interaction Problems with Non-Matching Discrete Interface: Momentum and Energy Conservation, Optimal Discretization and Application to Aeroelasticity," *Computer Methods and Applied Mechanical Engineering*, Vol. 157, No. 1, 1998, pp. 95–114.

[32]Pirzadeh, S. Z., "Advanced Unstructured Grid Generation for Complex Aerodynamic Applications," *26th AIAA Applied Aerodynamics Conference*, No. 7178, 2008.

[33]Bartels, R. E., Vatsa, V., Carlson, J.-R., Park, M., and Mineck, R., "FUN3D Grid Refinement and Adaptation Studies for the Ares Launch Vehicle," *28th AIAA Applied Aerodynamics Conference*, No. 4372, 2010.

[34]Hanson, P. W. and Doggett, R. V. J., "Aerodynamic Damping of a 0.02-Scale Saturn SA-1 Model Vibrating in the First Free-Free Bending Mode," NASA Technical Note NASA TN D-1956, 1963.

Appendix

The matrices $[T_y]$ and $[T_z]$ used in equations 14 and 15 relate the y and z displacements to the local angles of sideslip and attack. They are defined by

$$[T_y] = \begin{bmatrix} 0 & 1 & 0 & & 0 & 0 & 0 \\ & \vdots & & \ddots & & \vdots & \\ 0 & 0 & 0 & & 0 & 1 & 0 \end{bmatrix} \quad , \quad [T_z] = \begin{bmatrix} 0 & 0 & 1 & & 0 & 0 & 0 \\ & \vdots & & \ddots & & \vdots & \\ 0 & 0 & 0 & & 0 & 0 & 1 \end{bmatrix} \tag{20}$$

are $3N_{ll} \times N_{ll}$ matrices. The $N_{ll} \times 3N_{ll}$ matrix $\left[\hat{S}\right]$ relates the y and z modal displacements to the matrices $\partial\left[\hat{c}\right]/\partial\alpha$ and $\partial\left[\hat{c}\right]/\partial\beta$. $\left[\hat{S}\right]$ is defined

$$\left[\hat{S}\right] = \begin{bmatrix} 1 & 0 & \cdots & 0 & 0 \\ 1 & 0 & \cdots & 0 & 0 \\ 1 & 0 & \cdots & 0 & 0 \\ 0 & 1 & \cdots & 0 & 0 \\ 0 & 1 & \cdots & 0 & 0 \\ 0 & 1 & \cdots & 0 & 0 \\ & & \ddots & & \\ 0 & 0 & \cdots & 1 & 0 \\ 0 & 0 & \cdots & 1 & 0 \\ 0 & 0 & \cdots & 1 & 0 \\ 0 & 0 & \cdots & 0 & 1 \\ 0 & 0 & \cdots & 0 & 1 \\ 0 & 0 & \cdots & 0 & 1 \end{bmatrix} \tag{21}$$

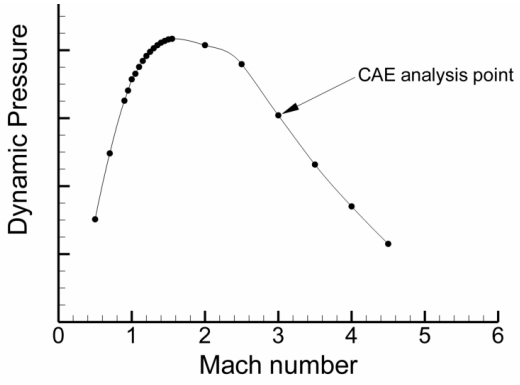

Figure 1. Trajectory and analysis points

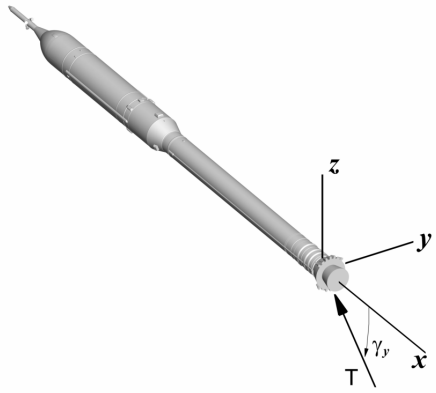

Figure 2. Coordinate system and gimbal angle definition

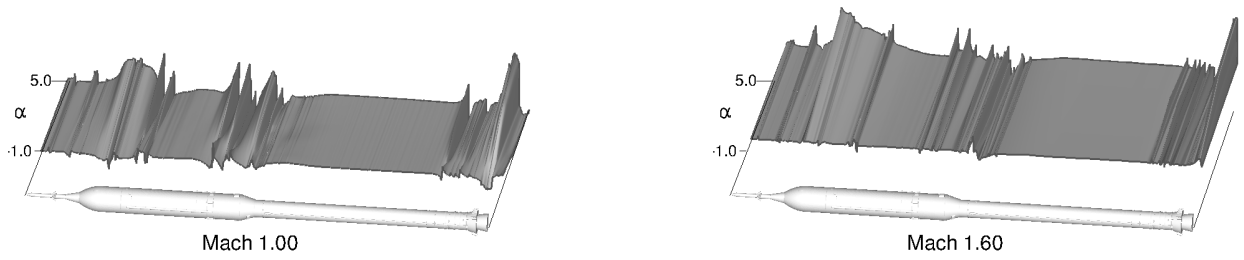

(a) Data generated with FUN3D

(b) Data generated with USM3D

Figure 3. Ares I CFD generated Cz response surfaces

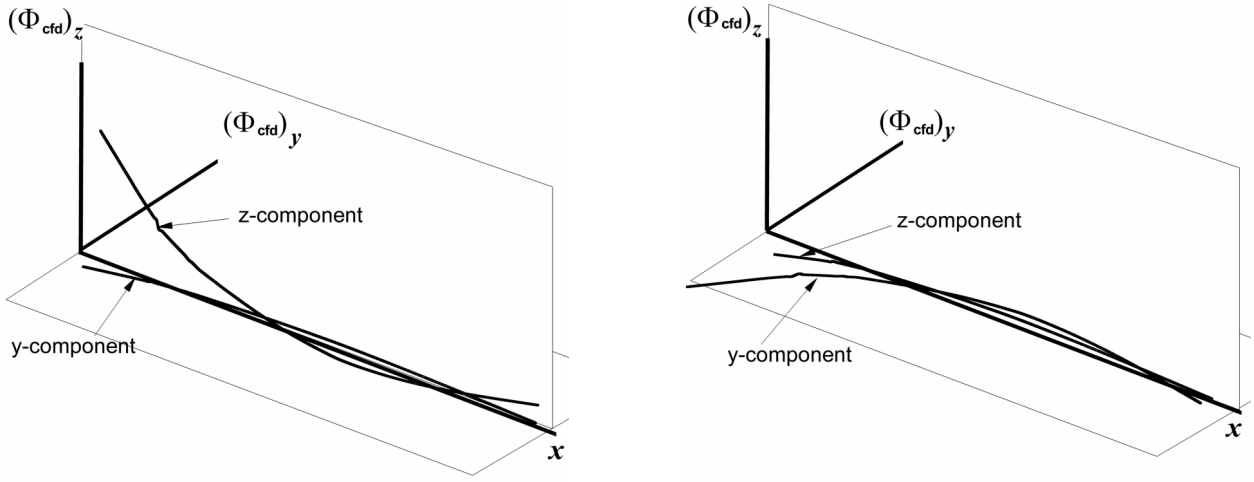

(a) Mode 1

(b) Mode 2

Figure 4. Ares I first bending modes

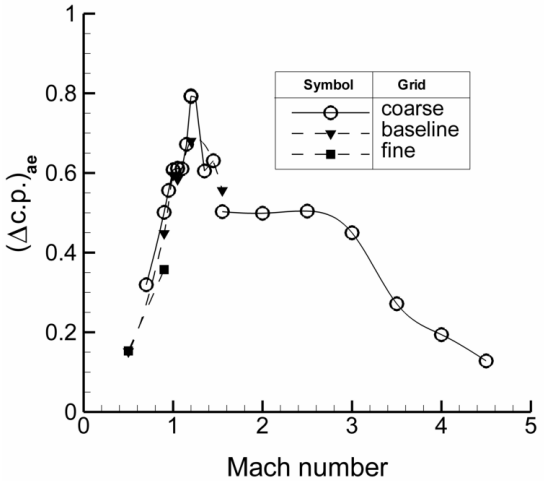

Figure 5. Effect of grid resolution on Ares I $(\Delta c.p.)_{ae}$, AIIM1 model, at q_{nom}

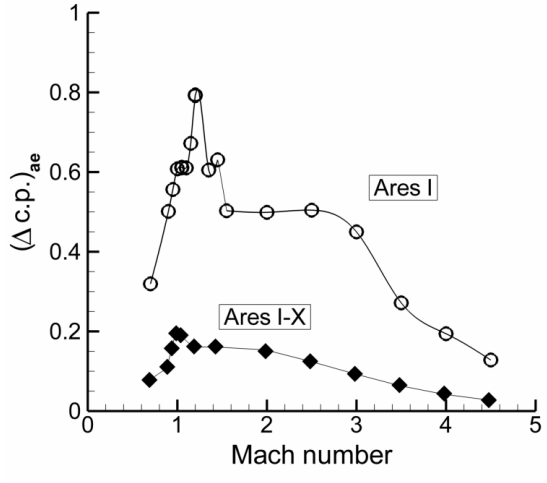

Figure 6. Comparison of $(\Delta c.p.)_{ae}$, coarse grid, at q_{nom} and $\alpha = 2.5$ deg.

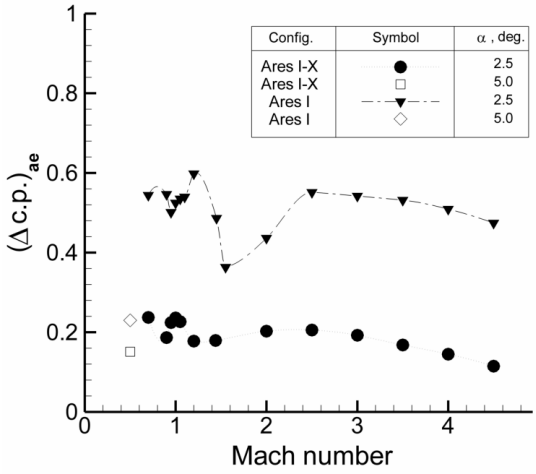

Figure 7. $\Delta c.p.$ due to thrust ($\gamma_y = 1$ deg.), coarse grid

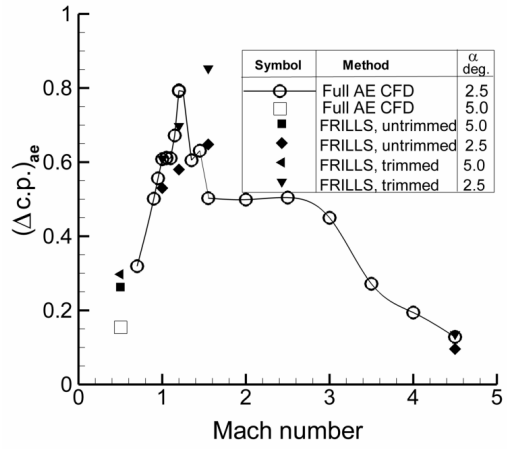

Figure 8. Effect of trim on Ares I $(\Delta c.p.)_{ae}$, coarse grid , AIIM1 model, q_{nom}

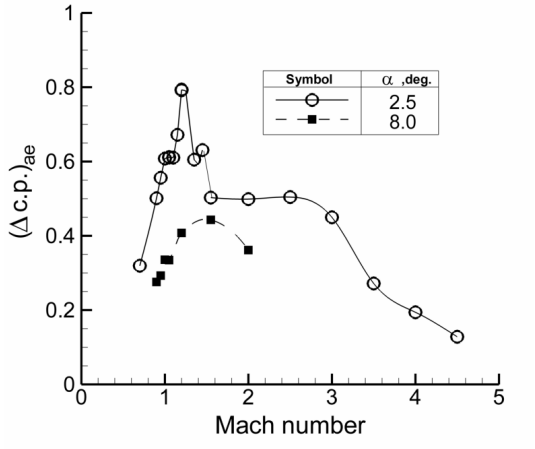

Figure 9. Effect of angle of attack on Ares I $(\Delta c.p.)_{ae}$, coarse grid, AIIM1 model, at q_{nom}.

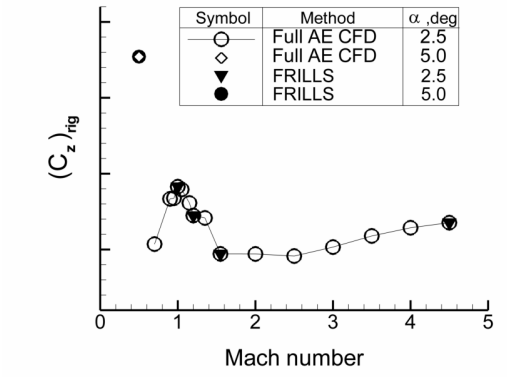

(a) $(C_z)_{rig}$

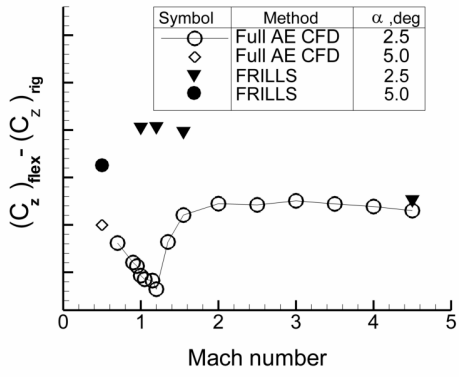

(b) ΔC_z, AIIM1, q_{nom}

Figure 10. Ares I force coefficients and increments, coarse grid, AIIM1 model, q_{nom}

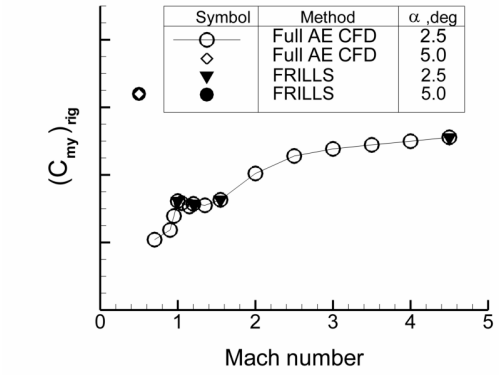

(a) $(C_{my})_{rig}$

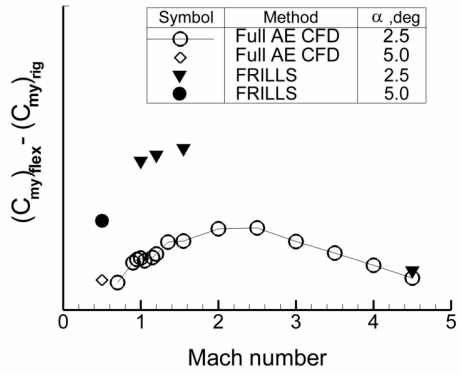

(b) ΔC_{my}, AIIM1, q_{nom}

Figure 11. Ares I moment coefficients and increments, coarse grid, AIIM1 model, q_{nom}

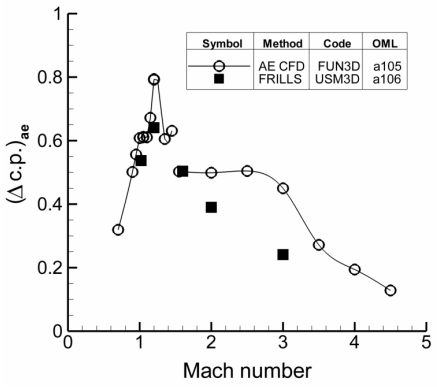

(a) Method/Code and OML Comparison, $\alpha = 2.5$ deg.

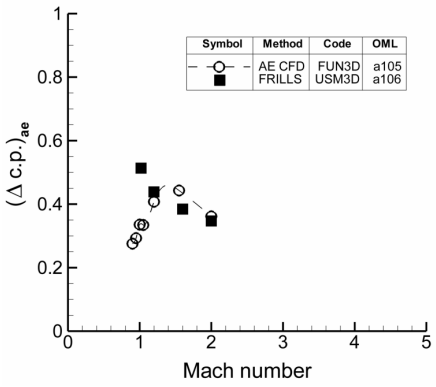

(b) Method/Code and OML Comparison, $\alpha = 8$ deg.

Figure 12. Flexibility induced $\Delta c.p.$ for Ares I, AIIM1 model, q_{nom}

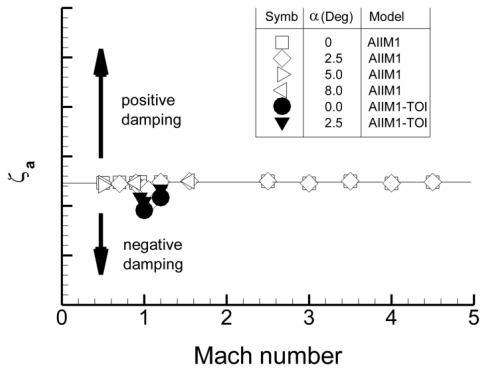

Figure 13. Ares I damping based on initial growth, coarse grid, q_{nom}

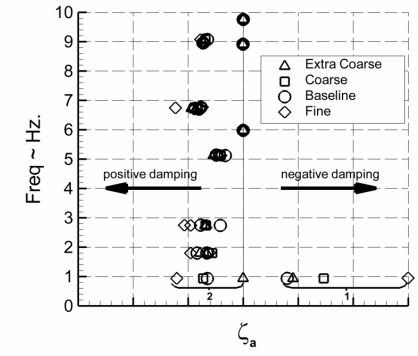

Figure 14. Ares I damping based on initial growth (modes 1, 2 identified), Mach 1.00**,** $\alpha = 0$ **deg., AIIM1-TOI model,** q_{nom}

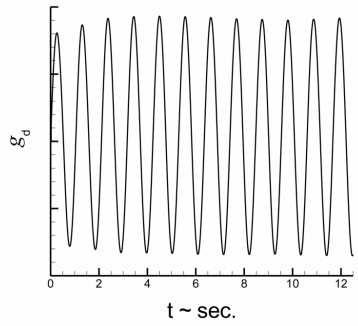

Figure 15. Ares I generalized displacement versus time, fine grid, Mach 1.00**,** $\alpha = 0$ **deg., AIIM1-TOI model,** q_{nom}

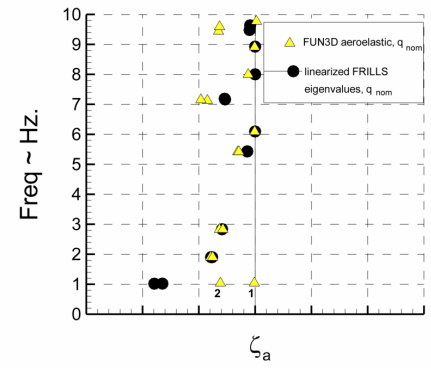

(a) Mach 1.2

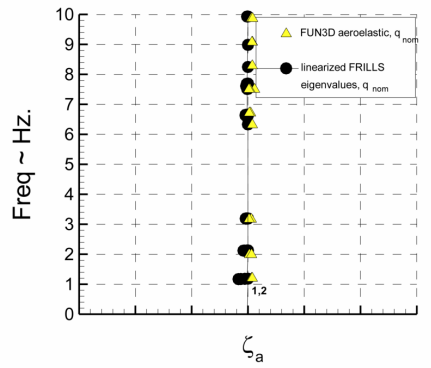

(b) Mach 4.5

Figure 16. Ares I damping based on initial growth, coarse grid, $\alpha = 0$ **deg., AIIM1 model** q_{nom}

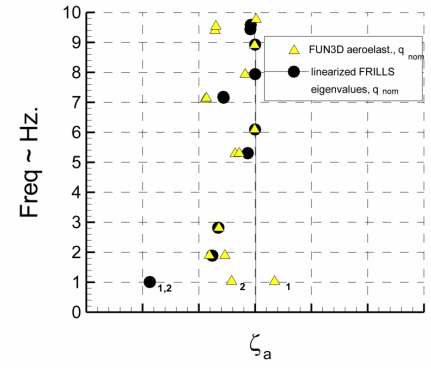

(a) AIIM1 model

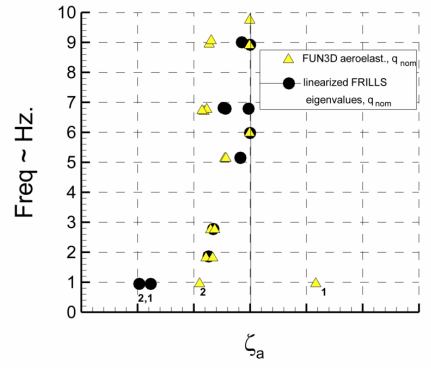

(b) AIIM1-TOI model

Figure 17. Ares I damping based on initial growth, coarse grid, Mach 1.00**,** $\alpha = 0$ **deg.,** q_{nom}

(a) OML with all protuberances

(b) OML with rings only

Figure 18. Ares I damping based on initial growth, coarse grid, Mach 1.00, $\alpha = 0$ **deg., AIIM1-TOI model**